Supplementary Information (SI) for Nanoscale.
This journal is © The Royal Society of Chemistry 2026

Supplemental information:
Stacking-Controlled Magnetic Exchange and Magnetoelectric Coupling in Bilayer CrI$_2$

B. Valdés-Toro,[1,*] I. Ferreira-Araya,[1,*] R. A. Gallardo,[1] and J. W. González[2,†]
[1]*Departamento de Física, Universidad Técnica Federico Santa María,*
Av. España 1680, Casilla 110V, Valparaíso, Chile
[2]*Departamento de Física, Universidad de Antofagasta,*
Av. Angamos 601, Casilla 170, Antofagasta, Chile
(Dated: February 12, 2026)

SI. ANTIFERROMAGNETIC ORDERS IN MONOLAYER CRI$_2$

Monolayer CrI$_2$ exhibits three competing collinear antiferromagnetic configurations: the ground state AF$_x$ (striped along x), AF$_y$ (striped along y), and the zigzag antiferromagnetic configuration AF$_z$, shown in Fig. S1. Magnetic symmetry analysis identifies AF$_x$ as type-I (MSG No. 56), while both AF$_y$ and AF$_z$ belong to type-IV (MSG No. 78). DFT calculations reveal a distinct energetic hierarchy, $E_{\mathrm{AF}_x} < E_{\mathrm{AF}_z} < E_{\mathrm{AF}_y}$, with AF$_z$ and AF$_y$ lying $+4.85\,\mathrm{meV/Cr}$ and $+5.49\,\mathrm{meV/Cr}$ above the ground state, respectively. This stability ordering originates from the interplay between the magnetic topology and the dimerized structure of the Cr sublattice, which features short intra-chain bonds ($d = 3.878\,\text{Å}$) and long inter-chain diagonal bonds ($d = 4.115\,\text{Å}$), details in Fig. S2. To rationalize the energy differences, we employ a nearest-neighbor Ising Hamiltonian based on the exchange pathways of the AF$_x$ reference state:

$$\mathcal{H} = -J_s \sum_{\langle i,j\rangle_{\mathrm{short}}} S_i S_j - J_l \sum_{\langle i,j\rangle_{\mathrm{long}}} S_i S_j, \tag{S1}$$

where $S_i = \pm 1$ represents the spin at site i. The exchange parameters extracted from Table II are $J_s = +2.56\,\mathrm{meV}$ (ferromagnetic, short bonds) and $J_l = -3.66\,\mathrm{meV}$ (antiferromagnetic, long bonds). Within this minimal model, the competition between ferromagnetic short-bond interactions and antiferromagnetic long-bond interactions naturally reproduces the energetic hierarchy $E_{\mathrm{AF}_x} < E_{\mathrm{AF}_z} < E_{\mathrm{AF}_y}$ obtained from the DFT calculations. This Ising model is intended as an effective description with unit spins; the physical Cr moment ($\sim 4\,\mu_B$, corresponding to $S \approx 2$) rescales the absolute magnitude of the exchange constants by a factor $1/S^2$, without affecting the relative energy hierarchy discussed here.

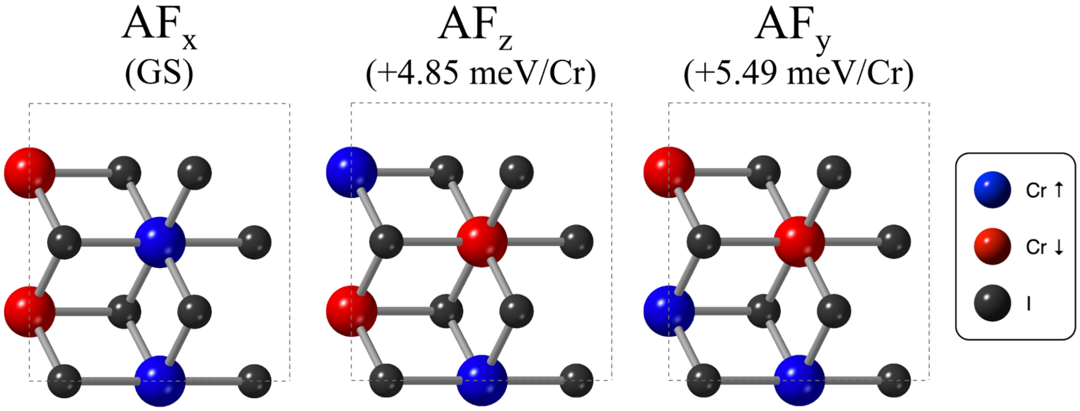

FIG. S1. Collinear antiferromagnetic configurations of the CrI$_2$ monolayer in a rectangular supercell. The stripe antiferromagnetic ground state AF$_x$ **(left)**, the zigzag antiferromagnetic configuration AF$_z$ **(center)**, and the stripe antiferromagnetic configuration AF$_y$ **(right)**. Numbers in parentheses indicate the energy difference relative to the AF$_x$ ground state, expressed in meV per Cr atom. Blue (red) spheres denote Cr atoms with spin up (down), while black spheres represent iodine atoms.

---

[*] These authors contributed equally to this work.

[†] Corresponding author:; jhon.gonzalez@uantof.cl

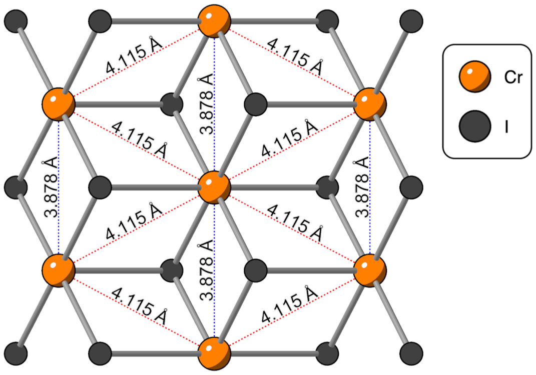

FIG. S2. Top view of the CrI$_2$ monolayer showing the inequivalent nearest-neighbor Cr–Cr distances. Blue (red) dotted lines indicate short (long) Cr–Cr bonds of length 3.878 Å (4.115 Å), respectively. These two distinct bond lengths define the competing ferromagnetic and antiferromagnetic exchange pathways discussed in the main text. Orange spheres denote Cr atoms and dark gray spheres represent iodine atoms.

SII. CALCULATION OF MAGNETIC EXCHANGE PARAMETERS USING OPENMX AND TB2J

Magnetic exchange interactions are computed using the Green's-function formalism combined with the magnetic force theorem (MFT), as implemented in the TB2J package [1]. The magnetic energy is mapped onto a classical Heisenberg Hamiltonian describing bilinear interactions between localized magnetic moments:

$$E = -\sum_{i \neq j} \left[J_{ij}^{\mathrm{iso}} \, \vec{S}_i \cdot \vec{S}_j + \vec{S}_i \, \mathbf{J}_{ij}^{\mathrm{ani}} \, \vec{S}_j + \vec{D}_{ij} \cdot (\vec{S}_i \times \vec{S}_j) \right], \tag{S2}$$

where $\vec{S}_i$ are normalized spin vectors ($|\vec{S}_i| = 1$), J_{ij}^{iso} is the isotropic Heisenberg exchange, $\mathbf{J}_{ij}^{\mathrm{ani}}$ is the symmetric anisotropic exchange tensor, and $\vec{D}_{ij}$ is the Dzyaloshinskii–Moriya interaction (DMI) vector. This Hamiltonian is equivalent to the tensorial form used internally by TB2J,

$$E = -\sum_{i \neq j} \vec{S}_i^T \mathbf{J}_{ij} \vec{S}_j,$$

with $\mathbf{J}_{ij} = J_{ij}^{\mathrm{iso}} \mathbf{I} + \mathbf{J}_{ij}^{\mathrm{ani}} + \mathbf{A}(\vec{D}_{ij})$, where $\mathbf{A}(\vec{D}_{ij})$ is the antisymmetric matrix associated with the DMI.

The calculation proceeds in two steps. First, self-consistent DFT+U calculations are performed using the OpenMX code [2, 3], which employs a localized pseudo-atomic orbital basis. The Hubbard U correction is applied to the Cr-3d states within the rotationally invariant formalism [4]. Both scalar-relativistic and fully relativistic (including spin-orbit coupling) calculations are performed to generate the Kohn-Sham Hamiltonian and overlap matrices for the reference magnetic configuration.

In the second step, TB2J evaluates the magnetic exchange parameters using the MFT. The method computes intermediate quantities A_{ij}^{uv} ($u, v = x, y, z$), obtained from the Green's functions of the system, as described in Eqs. (15)–(17) of Ref. [1]. These quantities are subsequently combined to yield the isotropic exchange J_{ij}^{iso}, the symmetric anisotropic tensor $\mathbf{J}_{ij}^{\mathrm{ani}}$, and the DMI vector $\vec{D}_{ij}$. In particular, the isotropic exchange parameter is given by the Liechtenstein formula [5]:

$$J_{ij}^{\mathrm{iso}} = -\frac{1}{4\pi} \, \mathrm{Im} \int_{-\infty}^{E_F} dE \, \mathrm{Tr} \left[\Delta_i \, \mathbf{G}_{ji}^{\uparrow}(E) \, \Delta_j \, \mathbf{G}_{ij}^{\downarrow}(E) \right], \tag{S3}$$

where E_F is the Fermi energy, $\Delta_i = \mathbf{H}_i^{\downarrow} - \mathbf{H}_i^{\uparrow}$ is the on-site exchange splitting, and $\mathbf{G}_{ij}^{\sigma}(E)$ is the spin-resolved Green's function between sites i and j. The anisotropic exchange and DMI terms are obtained from relativistic generalizations of this expression following the TB2J formalism.

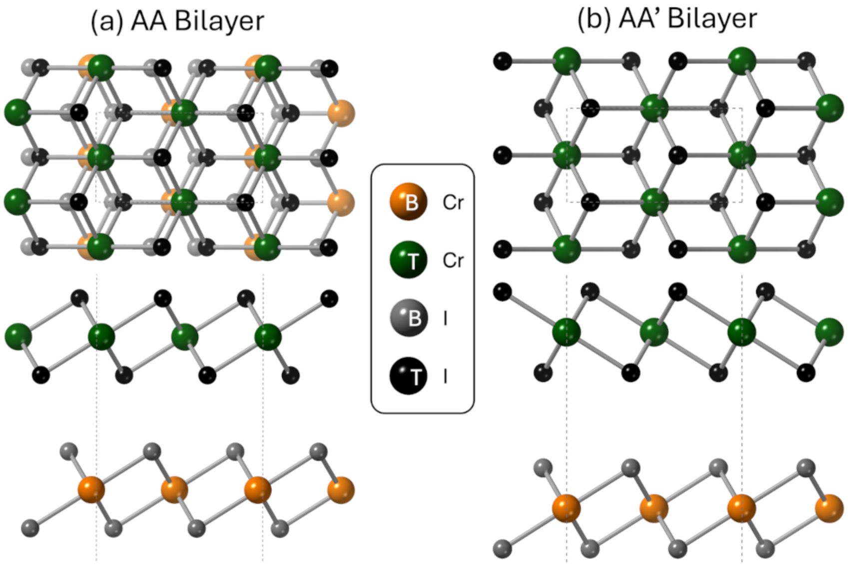

FIG. S3. Atomic structures of AA-like CrI_2 bilayers. Top and side views of the **(a)** direct AA stacking (centrosymmetric) and **(b)** indirect AA′ stacking (non-centrosymmetric), obtained from fully relaxed DFT geometries. Chromium atoms in the top (bottom) layer are shown in green (orange); iodine atoms are depicted in dark (light) gray to highlight the distinct vertical alignment of the I sublattices in each configuration.

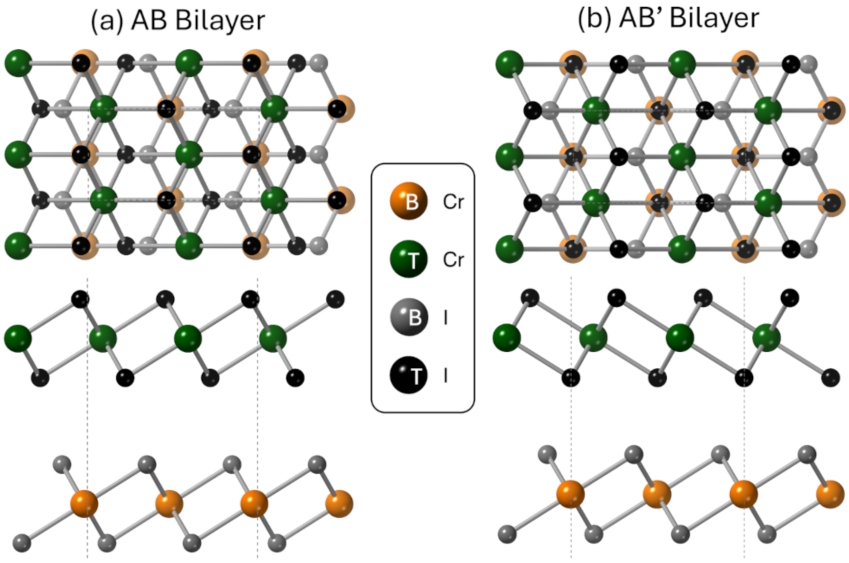

FIG. S4. Atomic structures of AB-like CrI_2 bilayers. Top and side views of the **(a)** direct AB stacking (centrosymmetric) and **(b)** indirect AB′ stacking (non-centrosymmetric), obtained from fully relaxed DFT geometries. The color scheme follows that of Fig. S3.

SIII. SYMMETRY ANALYSIS AND ORIGIN OF EXCHANGE-INDUCED BAND SPLITTINGS IN CRI$_2$ BILAYERS

The magnetic space groups and crystallographic symmetries of all relaxed CrI_2 bilayer configurations were determined using the `spglib` library (v2.6) with an atomic displacement tolerance of 0.01 Å. This tolerance reflects a balance between accurately identifying crystallographic symmetries and accommodating minor atomic displacements arising from full structural relaxation. Such a criterion ensures that the assigned symmetries reflect the true physical stacking registry of the relaxed bilayers rather than idealized geometries.

The AA-like bilayers shown in Fig. S3 are classified as centrosymmetric for the direct AA stacking, belonging to the space group $C2/m$ (No. 12), while the corresponding indirect AA′ stacking is non-centrosymmetric and belongs to the

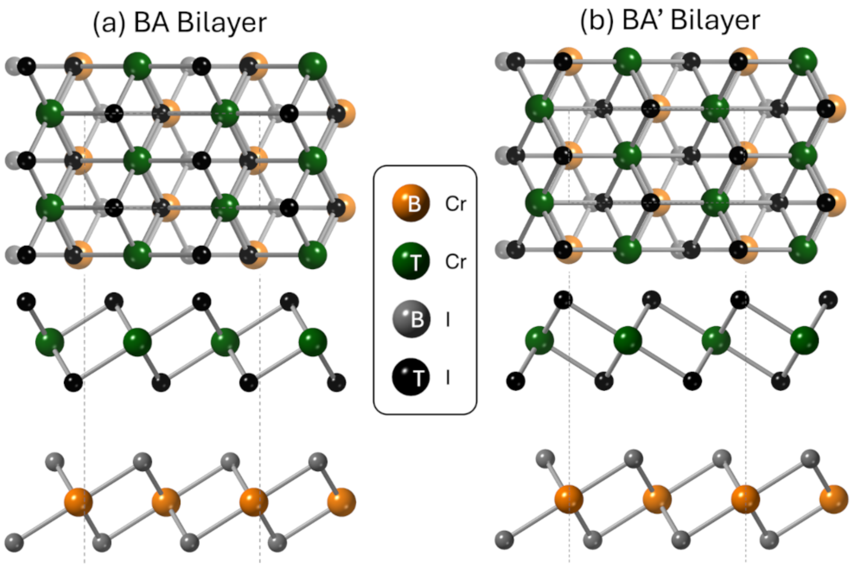

FIG. S5. Atomic structures of BA-like CrI$_2$ bilayers. Top and side views of the **(a)** direct BA stacking (centrosymmetric) and **(b)** indirect BA′ stacking (non-centrosymmetric), obtained from fully relaxed DFT geometries. The color scheme follows that of Fig. S3.

polar space group $Amm2$ (No. 38). Similarly, the AB-like bilayers presented in Fig. S4 preserve inversion symmetry in the direct AB stacking ($C2/m$, No. 12), whereas the indirect AB′ stacking breaks inversion symmetry and is classified within the space group Cm (No. 8). Finally, the BA-like bilayers shown in Fig. S5 follow the same symmetry trend: the direct BA stacking remains centrosymmetric and belongs to the space group $C2/m$ (No. 12). In contrast, the indirect BA′ stacking lacks inversion symmetry and is assigned to the space group Pm (No. 6). These symmetry distinctions have direct consequences for the electronic structure of the bilayers. In collinear antiferromagnets, band degeneracy is protected when the system possesses an effective antiunitary symmetry, most commonly the combined $\mathcal{PT}$ operation. More generally, any composite symmetry formed by a spatial operation combined with time reversal can enforce Kramers-like degeneracy throughout the Brillouin zone, even in the absence of spin-orbit coupling.

In indirect stackings such as BA′, the layer registry breaks global inversion symmetry ($\mathcal{P}$). When this structural asymmetry is combined with a collinear antiferromagnetic order that breaks time-reversal symmetry ($\mathcal{T}$), the protecting $\mathcal{PT}$ symmetry is lost. As a result, the exchange interaction operates within a polar crystal environment, allowing for finite and momentum-dependent spin splittings in the electronic band structure. This mechanism is fully captured at the non-relativistic level and does not rely on spin-orbit coupling, demonstrating that the splittings are purely exchange-driven in origin. As confirmed by the real-space spin-density distributions shown in Fig. S6, the Cr magnetic moments remain fully compensated and equal in magnitude in both monolayer and bilayer configurations, with only negligible differences at the fourth decimal place. The lifting of spin degeneracy, therefore, does not originate from inequivalent local moments on the two antiferromagnetic sublattices, but from symmetry breaking at the level of the crystal stacking. The magnitude of these exchange-induced splittings is relatively small (on the order of a few meV), which makes them difficult to resolve in the full band dispersion. To explicitly illustrate this effect, Fig. S7 presents a magnified view of the valence-band region for the BA′ bilayer (space group Pm (No. 6)) in the antiparallel interlayer configuration ($\uparrow\downarrow$ / $\downarrow\uparrow$). The zoomed-in bands clearly reveal the lifting of spin degeneracy near the valence-band maximum, confirming the presence of exchange-induced splittings.

Taken together, these results demonstrate that the observed band splittings originate from exchange interactions in a non-centrosymmetric antiferromagnetic environment. The symmetry analysis presented above shows that none of the CrI$_2$ bilayer stackings considered in this work realize the non-relativistic spin-group symmetries required for altermagnetism, namely crystallographic operations that map opposite-spin sublattices onto each other while inverting momentum ($\mathbf{k} \to -\mathbf{k}$). Consequently, the observed splittings arise from exchange physics in a polar antiferromagnet and should not be interpreted as signatures of altermagnetic order.

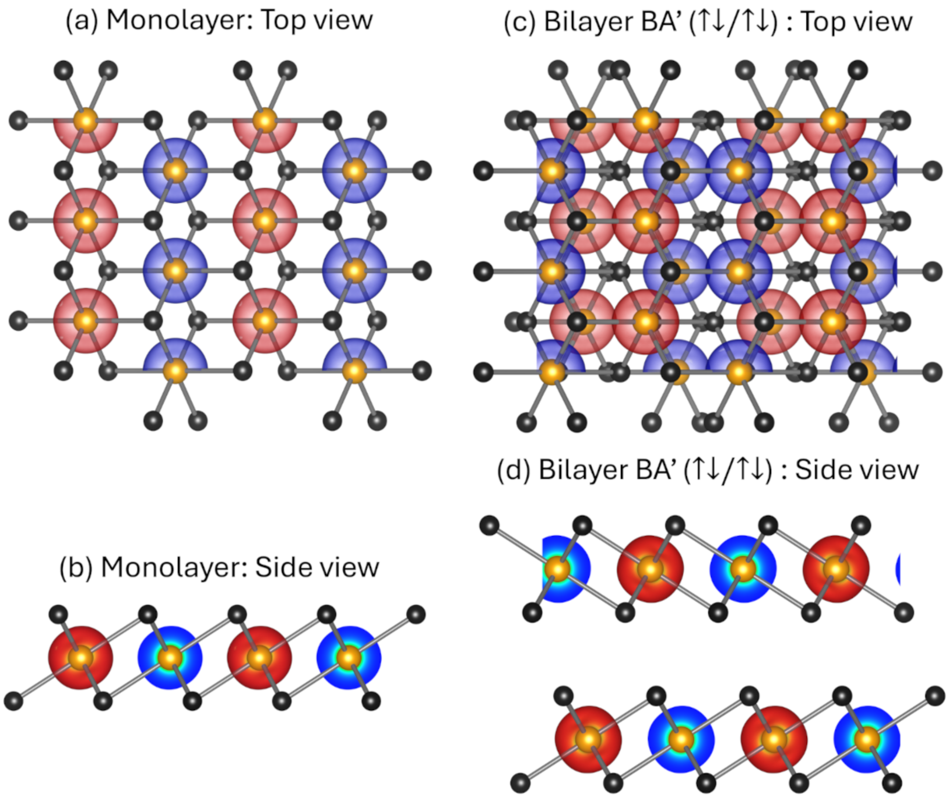

FIG. S6. Real-space spin density distribution $(\rho_\uparrow - \rho_\downarrow)$ of the CrI$_2$ monolayer in the AF$_x$ configuration and of the BA$'$ bilayer in the antiparallel interlayer configuration (↑↓ / ↓↑). Panels (a) and (b) show the top and side views of the AF$_x$ monolayer, respectively, while panels (c) and (d) display the corresponding top and side views of the BA$'$ bilayer. Red and blue isosurfaces correspond to positive and negative spin polarization, respectively, plotted at an isovalue of 0.009 $e^-/\text{Å}^3$.

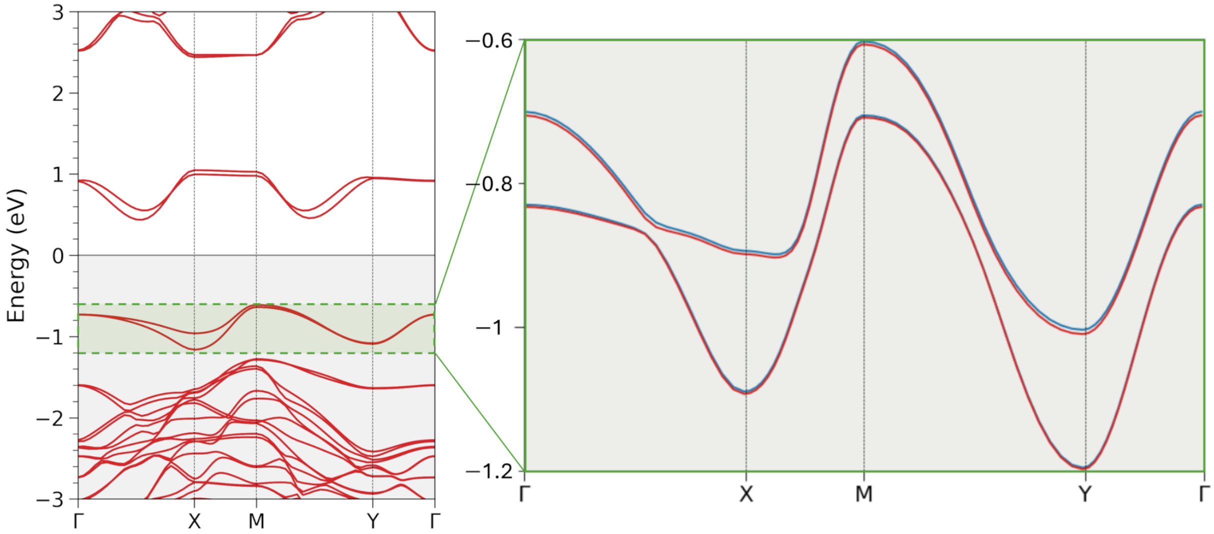

FIG. S7. Zoomed-in electronic band structure of the BA$'$ bilayer CrI$_2$ in the antiparallel interlayer configuration (↑↓ / ↓↑). The band structure shown on the left corresponds to the full dispersion reported in Fig. 3 of main text, while the right panel displays a magnified view of the energy window highlighted by the green shaded region. Blue and red curves denote bands associated with opposite spin channels, revealing the small exchange-induced splittings near the valence-band maximum. Note that the splittings are on the order of a few meV and are therefore not easily resolved in the full band dispersion. The Fermi level is set to zero energy.

---

[1] X. He, N. Helbig, M. J. Verstraete, and E. Bousquet, Tb2j: A python package for computing magnetic interaction parameters, Computer Physics Communications **264**, 107938 (2021).

[2] T. Ozaki, Variationally optimized atomic orbitals for large-scale electronic structures, Physical Review B **67**, 155108 (2003).

[3] T. Ohwaki, M. Otani, and T. Ozaki, A method of orbital analysis for large-scale first-principles simulations, The Journal of Chemical Physics **140** (2014).

[4] M. Cococcioni and S. De Gironcoli, Linear response approach to the calculation of the effective interaction parameters in the LDA+U method, Physical Review B **71**, 035105 (2005).

[5] A. I. Liechtenstein, M. Katsnelson, V. Antropov, and V. Gubanov, Local spin density functional approach to the theory of exchange interactions in ferromagnetic metals and alloys, Journal of Magnetism and Magnetic Materials **67**, 65 (1987).